remote sensing

MDPI

Article

Radiometric Calibration Evaluation for FY3D MERSI-II Thermal Infrared Channels at Lake Qinghai

Lin Yan [1,2], Yonghong Hu [1,*], Yong Zhang [3], Xiao-Ming Li [1], Changyong Dou [1], Jun Li [2], Yidan Si [3] and Lijun Zhang [3]

[1] Key Laboratory of Digital Earth Science, Aerospace Information Research Institute, Chinese Academy of Sciences, Beijing 100094, China; yanlin7@mail2.sysu.edu.cn (L.Y.); lixm@radi.ac.cn (X.-M.L.); doucy@aircas.ac.cn (C.D.)

[2] School of Geography and Planning, Sun Yat-sen University, Guangzhou 510275, China; lijun48@mail.sysu.edu.cn

[3] National Satellite Meteorological Center, China Meteorological Administration, Beijing 100081, China; zhangyong@cma.gov.cn (Y.Z.); siyd@cma.gov.cn (Y.S.); zhanglj@cma.gov.cn (L.Z.)

* Correspondence: huyh01@radi.ac.cn

Abstract: The absolute radiometric accuracy of the Fengyun 3D advanced Medium Resolution Spectral Imager (FY3D MERSI-II) thermal infrared bands was evaluated using the collected field measurements and atmospheric transfer simulations during 16–22 August 2019 at Lake Qinghai. A thermal infrared radiometer equipped on an unmanned surface vehicle was used to continuously collect the water temperature. Atmospheric conditions, surface emissivity, and aerosol optical depth measured near the field experiment site were adopted by the atmospheric transfer code to calculate the parameters about the influence of atmosphere on long-wave radiation, including the path radiance and the transmittance propagated from land surface to the satellite. The radiometric calibration accuracy analysis suggests that the differences between the simulated brightness temperature and satellite-based brightness temperature are −0.346 K and −0.722 K for channel 24 on 18 and 20 August, respectively, while it reaches −0.460 K and −1.036 K for channel 25 on 18 and 20 August, respectively. The vicarious calibration coefficients were found to be in good agreement with the internal onboard calibration coefficient in channel 24 and 25 of the FY3D MERSI-II according to the validation analysis in selected regions. The thermal infrared bands of the FY3D have a good in-orbit operational status according to our vicarious calibration experiments.

Keywords: radiometric calibration; FY3D; thermal infrared bands; lake qinghai

Citation: Yan, L.; Hu, Y.; Zhang, Y.; Li, X.-M.; Dou, C.; Li, J.; Si, Y.; Zhang, L. Radiometric Calibration Evaluation for FY3D MERSI-II Thermal Infrared Channels at Lake Qinghai. *Remote Sens.* **2021**, *13*, 466. https://doi.org/10.3390/rs13030466

Received: 27 November 2020
Accepted: 22 January 2021
Published: 28 January 2021

1. Introduction

The thermal infrared (TIR) spectrum can delineate the characterization about emitted radiation information from the Earth's surface, which plays important roles in cloud recognition [1,2], surface temperature inversion [3–5], and the surface radiation budget [6–8]. Long-term consistent land surface temperature datasets with excellent calibration accuracy are the basis for analyzing environment evolution and climate change [9–11]. Well-calibrated sensors are capable of receiving climate change signals with high accuracy and stability, and the derived remote sensing products are key to understand the mechanism of environment evolution and climate change [9]. Therefore, reasonable radiometric calibrations are important to maintain the accuracy of thermal infrared images and their quantitative applications [12]. Absolute radiometric calibration usually consists of three parts, including laboratory calibration, onboard calibration, and vicarious calibration [13–15]. All the fundamental indicators related to the specifications are thoroughly tested in the laboratory to meet the preparatory requirements. The onboard calibration coefficients for the thermal infrared channels are usually derived from the onboard calibration system,

including onboard blackbody and deep space observations. However, calibration coefficients obtained at the laboratory and from the onboard calibration system might be changed due to the degraded detector or the influence from the space environment, resulting in instability in the radiometric calibration accuracy [16,17]. Therefore, vicarious calibration campaigns are usually adopted to validate and evaluate the radiometric calibration accuracy. Currently, ground-based vicarious radiometric calibration is regarded as an effective way to conduct the absolute radiometric calibration for TIR sensors.

Stable targets are usually used as the calibration sites for the vicarious calibration of TIR bands, including deep convective clouds [18–20], ice sheets [21,22], oceans [23,24], and lakes [15,25–28]. Large lakes with higher elevation are considered to be ideal radiometric calibration sites because of their high spatial uniformity, lower surface temperature variation, and suitable atmospheric conditions [15,26]. Surface parameters could be obtained by airborne sensors [29], buoys [30,31], and boats [15,25]. A well-calibrated infrared line scanner mounted on an aircraft can capture a high-quality image at the time of satellite overpass. This approach has less uncertainty induced by the atmosphere, but it has two limitations: (1) the calibration accuracy is limited by the calibration uncertainty of the aerial instruments; and (2) higher costs of the concurrent experiment by aircraft [29,32,33]. Continuous bulk temperature and atmospheric conditions recorded by buoys are also useful for predicting at-sensor radiance, but bulk temperature would introduce errors into a calibration analysis because buoys only collect water temperature at a fixed depth [15,30,33]. Temperature records observed by a radiometer mounted on the boat is an optimized method for conducting vicarious calibration experiments, and at-sensor radiance could be predicted by the moderate spectral resolution atmospheric transmittance algorithm with the field measurement information from the atmospheric profile and surface emissivity [33].

Compared to the Multichannel Visible IR Scanning Radiometer (MVIRS) on board Fengyun−1, the Medium Resolution Spectral Imager (MERSI) on board Fengyun−3 (FY−3) series satellites has significant improvements in spectral channels, radiometric calibration accuracy, sounding capabilities, and spatial resolution [34–36]. MERSI is similar to the imaging instrument, the Visible Infrared Imaging Radiometer (VIIRS), on board the Joint Polar-orbit Satellite System (JPSS). The advanced Medium Resolution Spectral Imager (MERSI-II) on the Fengyun−3D (FY3D) can observe land surface targets at split-window regions with a spatial resolution of 250 m (Table 1) [37,38]. Pre-launch experiments for MERSI-II are used to obtain the specification parameters about its radiometric accuracy, such as the noise equivalent temperature difference (NEΔT) [39]. The onboard radiometric calibration system of MERSI-II TIR bands consists of the full-aperture onboard blackbody and space view, and the effective emissivity of the blackbody reaches 0.97 with its temperature monitored by seven evenly spaced precision thermometers [39].

Table 1. Specifications of the Fengyun 3D Advanced Medium Resolution Spectral Imager (FY3D MERSI-II).

Band Number	Center Wavelength (μm)	Bandwidth (nm)	Spatial Resolution (m)	SNR or NEΔT (K)	Maximum Reflectance ϱ or Dynamic Range (K)
1	0.47	50	250	100	90%
2	0.55	50	250	100	90%
3	0.65	50	250	100	90%
4	0.865	50	250	100	90%
5	1.38	20/30	1000	60/100	90%
6	1.64	50	1000	200	90%
7	2.13	50	1000	100	90%
8	0.412	20	1000	300	30%
9	0.443	20	1000	300	30%
10	0.49	20	1000	300	30%
11	0.555	20	1000	500	30%
12	0.67	20	1000	500	30%
13	0.709	20	1000	500	30%
14	0.746	20	1000	500	30%
15	0.865	20	1000	500	30%
16	0.905	20	1000	200	100%
17	0.936	20	1000	100	100%
18	0.940	50	1000	200	100%
19	1.030	20	1000	100	100%
20	3.800	180	1000	0.25 K	200–350 K
21	4.050	155	1000	0.25 K	200–350 K
22	7.200	500	1000	0.30 K	200–350 K
23	8.550	300	1000	0.25 K	200–350 K
24	10.800	1000	250	0.40 K	200–350 K
25	12.000	1000	250	0.40 K	200–350 K

The FY3D satellite has been in operation in orbit for more than three years since its launch on 15 November 2017. It is necessary to evaluate the absolute radiometric calibration accuracy of MERSI-II's TIR bands for the purpose of further understanding the possible influences of calibration uncertainties on its remote sensing products. Field campaigns at Lake Qinghai from 16 August to 22 August 2019 were carried out to evaluate the radiometric calibration status of the TIR channels of the FY3D MERSI-II. Section 2 and Section 3 introduce the calibration site and provide detailed information about radiometric calibration theory, methodology, materials, and data processing. Section 4 shows the results of the bias evaluation of operational calibration for the TIR bands of the FY3D MERSI-II and illustrates the validation results for the vicarious radiometric calibration coefficient in selected regions. We summarize those findings in the final section.

2. Calibration Site

As an important site of the China Radiometric Calibration Site (CRCS) in China, Lake Qinghai is located in the east of Qinghai Province and has a large homogeneous saltwater surface (Figure 1). It has an elevation of 3196 m above sea level and an area of 4635 km^2 (length 106 km, width 63 km, average depth 19 m). Lake Qinghai is considered to be an ideal calibration site for TIR instruments for the following reasons: (1) clear water with 4% reflectance at the visible band and 1% at the TIR band; (2) a relative uniform distribution of water temperature with a temperature variation of less than 1°C; (3) an alpine and semi-arid grassland climate with 112 clear days per year; and (4) a clear atmosphere with an aerosol optical depth less than 0.18 and an annual precipitation of about 434.5 mm [14,25,40]. Lake Qinghai has been used to successfully conduct radiometric calibration missions for many Chinese satellites since 1996, including FY-series satellites [15,25,40],

Huanjing satellites (HJ−1A/−1B) [28], and the China–Brazil earth resource satellite (CBERS) [41,42].

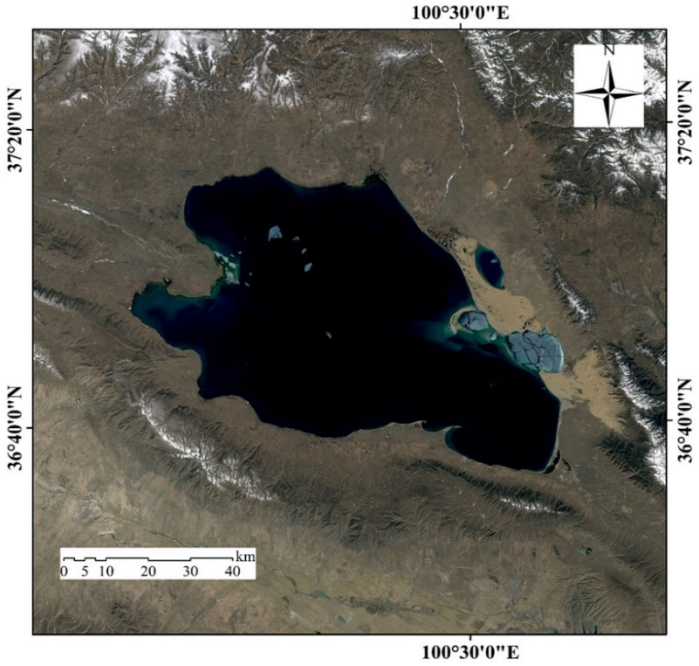

Figure 1. Location of Lake Qinghai. The true color image is created from a remote sensing image acquired on 17 April 2019 from Landsat 8 Operational Land Imager (OLI).

3. Methods

3.1. Theory of TIR Radiometric Calibration

The at-sensor radiance received by the TIR channels of the satellite sensor consists of three parts: the radiance emitted from the water and attenuated by the atmosphere, the path radiance that scattered from the atmosphere, and the radiance (i.e., downward radiance of the atmosphere and long-wave radiance of the Sun) reflected from the water and attenuated by the atmosphere [27,31,35]. Hence, the at-sensor radiance received by the sensor can be expressed as:

$$L_S(\lambda)=\tau_\alpha(\lambda)L_q(\lambda)+L_{path}(\lambda)+\tau_\alpha(\lambda)L_d(\lambda)\rho_q(\lambda), \quad (1)$$

where $L_S(\lambda)$ is the spectral radiance received by the sensor, $\tau_\alpha(\lambda)$ is the spectral transmittance of the atmosphere, $L_q(\lambda)$ is the radiance radiated from the water at the observation direction of the satellite, $L_{path}(\lambda)$ is the path radiance scattered from the atmosphere observed by the sensor, $L_d(\lambda)$ is the atmospheric downward radiance, and $\rho_q(\lambda)$ is the reflectance of the water surface. Because of the low water surface reflectance, the atmospheric downward radiance reflected from the water and attenuated by the atmosphere can be neglected. $\tau_\alpha(\lambda)$ and $L_{path}(\lambda)$ could be simulated by the moderate resolution atmospheric transmission code (MODTRAN 4.2).

The equivalent radiance ($L_{es}(\lambda)$) at the sensors' aperture can be obtained by convoluting the at-sensor spectral radiance with the relative spectral response (RSR), which is given as:

$$L_{es}(\lambda)=\frac{\int L_S(\lambda)\mathrm{RSR}(\lambda)d\lambda}{\int \mathrm{RSR}(\lambda)d\lambda}, \quad (2)$$

where $L_s(\lambda)$ is the spectral radiance calculated from Equation (1), and $\mathrm{RSR}(\lambda)$ is the relative spectral response of the channel. For the FY3D MERSI-II thermal channels, the conversion between the equivalent radiance and digital number (DN) is based on Equation (3):

$$L_{ob}(\lambda) = Gain(\lambda) \cdot DN_{ob}(\lambda) + Bias(\lambda), \quad (3)$$

where $Gain(\lambda)$ represents the gain of the calibration coefficient, $Bias(\lambda)$ is the bias of the calibration coefficients, and $DN_{ob}(\lambda)$ represents the digital number of observations from space view and in-situ measurements. Four pairs of $Gain(\lambda)$ and $L_{ob}(\lambda)$ were calculated by using the linear fitting between $DN_{ob}(\lambda)$ and $L_{ob}(\lambda)$ for channel 24 and 25 on August 18 and 20, respectively. Then, the in-situ radiometric calibration coefficients were validated by comparing the bright temperature based on in-situ calibration coefficients and operational calibration coefficients.

3.2. Surface Parameters Measured by an Unmanned Surface Vehicle

Surface temperatures were measured by a thermal infrared radiometer, the CE312-N1, manufactured by CIMEL Electronique, Paris, which was equipped at the top of an unmanned surface vehicle (USV), 2 m away from the boat edge (Figure 2). The CE312-N1 has four different spectral bands (8.0–14.0 μm, 8.2–9.2 μm, 10.3–11.3 μm, and 11.5–12.5 μm) and an observation accuracy of 0.10 K [43]. The solar-powered USV is capable of long-term cruising with the roof covered by solar cell film. It can work in automatic or manual navigation mode with the location information saved every 30 s by a global positioning system (GPS) module. Meanwhile, land-based subsystem monitors can record and transmit the track of the USV to the computer in real-time. In order to arrive at the appropriate location on the lake, the USV was released 2 h before the satellite overpass to continuously collect water surface temperature, air temperature, humidity, wind speed, and wind direction. Water temperature was measured over a wide-open area at the southeast part of Lake Qinghai (Figure 3). Due to the influence of cloud cover and atmospheric conditions, we selected in-situ measurements on 18 and 20 August to perform calibration analysis. According to the temperature variation along the navigation route of the USV from 14:00 to 15:30 on 18 August, the lake surface has a relatively consistent temperature change with its variation being less than 0.2 °C (Figure 3).

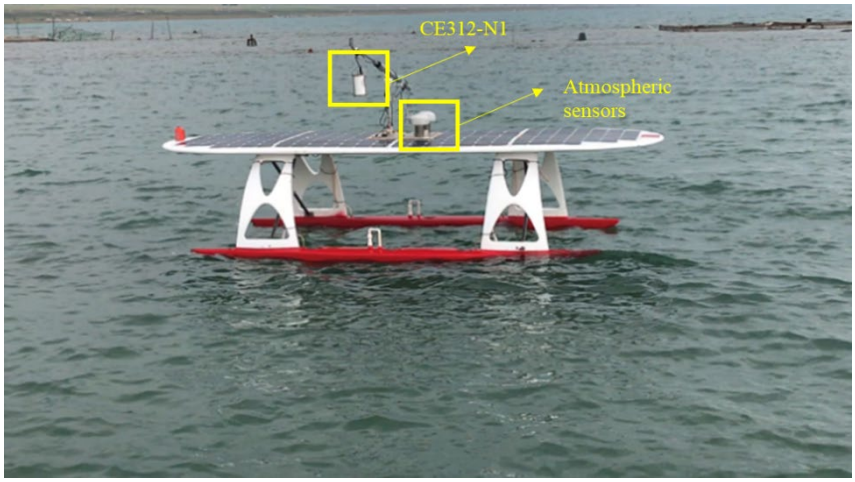

Figure 2. Unmanned surface vehicle with atmospheric sensors and a CE312-N1 used in the vicarious radiometric calibration.

The clear-day pixels in the MERSI-II images along the navigation track of the boat were selected during the concurrent experiments. Then, three steps were conducted to

convert the DN value of the image to the radiance or brightness temperature. First, the at-sensor radiance was derived from the DN according to the calibration coefficients for channel 24 and 25:

$$RAD = DN \times S + I, \tag{4}$$

where S and I are the slope and the intercept of the radiometric calibration coefficients, respectively. Here, S and I are 0.010 and 0.000, respectively. RAD is the at-sensor radiance with a unit of $\mathrm{mW/(m^2 \cdot cm^{-1} \cdot sr)}$.

Second, the Inverse Plank function was used to calculate the equivalent brightness temperature T_e.

$$T_e = \frac{C_2 \cdot \sigma}{\ln(C_1 \cdot \sigma^3) - \ln((RAD \cdot 10^7) + 1)}, \tag{5}$$

where T_e is the equivalent blackbody brightness temperature, and $C_1 = 1.191 \times 10^{-12}\ \mathrm{W/(cm^2 \cdot sr \cdot (cm^{-1})^4)}$ and $C_2 = 1.439\mathrm{K \cdot cm}$ are the first and second radiation constant, respectively. σ is the wavenumber ($\mathrm{cm^{-1}}$) determined by:

$$\sigma = 10000 / \lambda, \tag{6}$$

where λ is the effective center wavelength of channel 24 and 25, respectively (Table 1).

Then, brightness temperature was calculated by Equation (7):

$$BT = A \cdot T_e + B, \tag{7}$$

where A is 1.00133 and 1.00065 for channel 24 and 25 of the MERSI-II, respectively, and B is −0.05130 and 0.08750, respectively [44].

DN values from the deep-space view were also converted to the radiance according to the Planck equation and were then used to calculate the vicarious calibration coefficient by combining it with the predicted top-of-atmosphere (TOA) radiance by MODTRAN simulation.

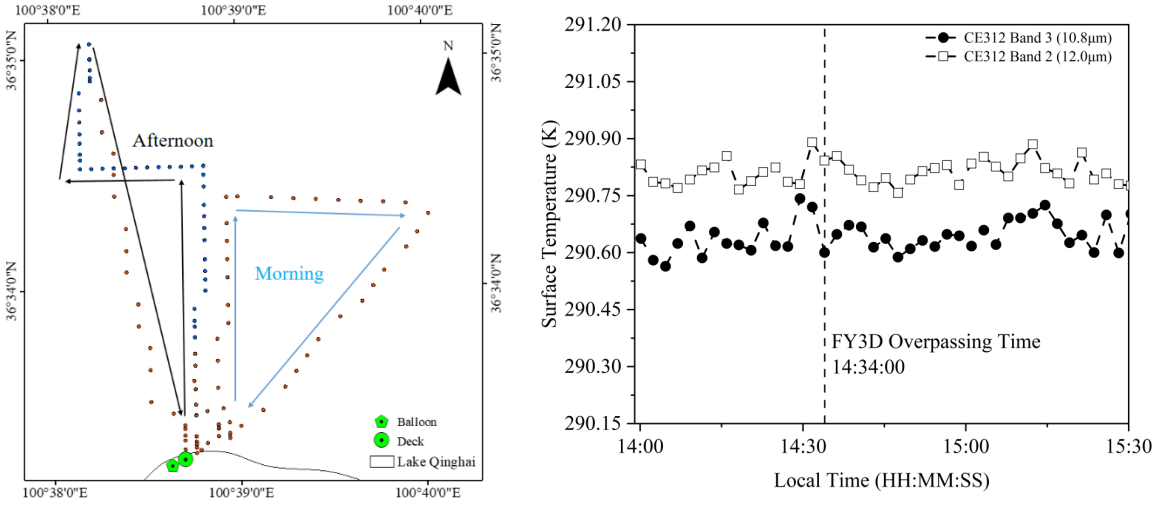

Figure 3. The surface temperature observed along the navigation route (**a**), and its variation during FY−3D MERSI-II overpass on 18 August 2019 (**b**).

3.3. Spectral Matching

The difference of the relative spectral response (RSR) among similar TIR channels will result in the bias of the derived brightness temperature, even when the same target is

observed at the same time [45]. Many efforts were devoted to eliminating these differences by applying the spectral band adjustment factor (SBAF) [45–47] and the matched-image adjustment factor (MIAF) [13]. There are small differences in the RSR of the TIR channels between the MERSI-II and the CE312 (Figure 4). In order to reduce the influence of RSR differences on the radiometric calibration accuracy, a series of MODTRAN simulations were adopted to create their spectral matching factors. First, we generated the top-of-atmosphere (TOA) radiance, including 9 surface types (cloud cover, desert, dry grass, field, forest, fresh snow, maple, ocean, wet grass), 2 satellite observing geometries (vertical, 10°), and 6 atmospheric profiles (Tropical, Mid-Latitude Summer/Winter, Sub-Arctic Summer/Winter, U.S. Standard) under 9 temperature situations (278K, 283K, 288K, 293K, 298K, 303K, 208K, 212K, 320K) (Table 2). Then, the equivalent TOA radiance was generated by convolving the RSR and simulated TOA radiance for the selected thermal infrared bands of the MERSI-II and the CE312. Linear regression was performed on the equivalent radiance at 972 points against the corresponding bands to obtain the spectral matching factors (Figure 5).

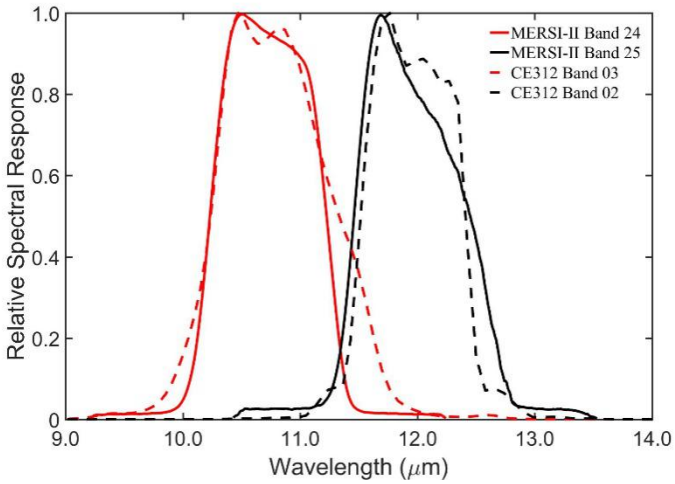

Figure 4. Relative spectral response of the FY−3D MERSI-II (channel 24 and channel 25) and the CE312 bands (band 3 and band 2).

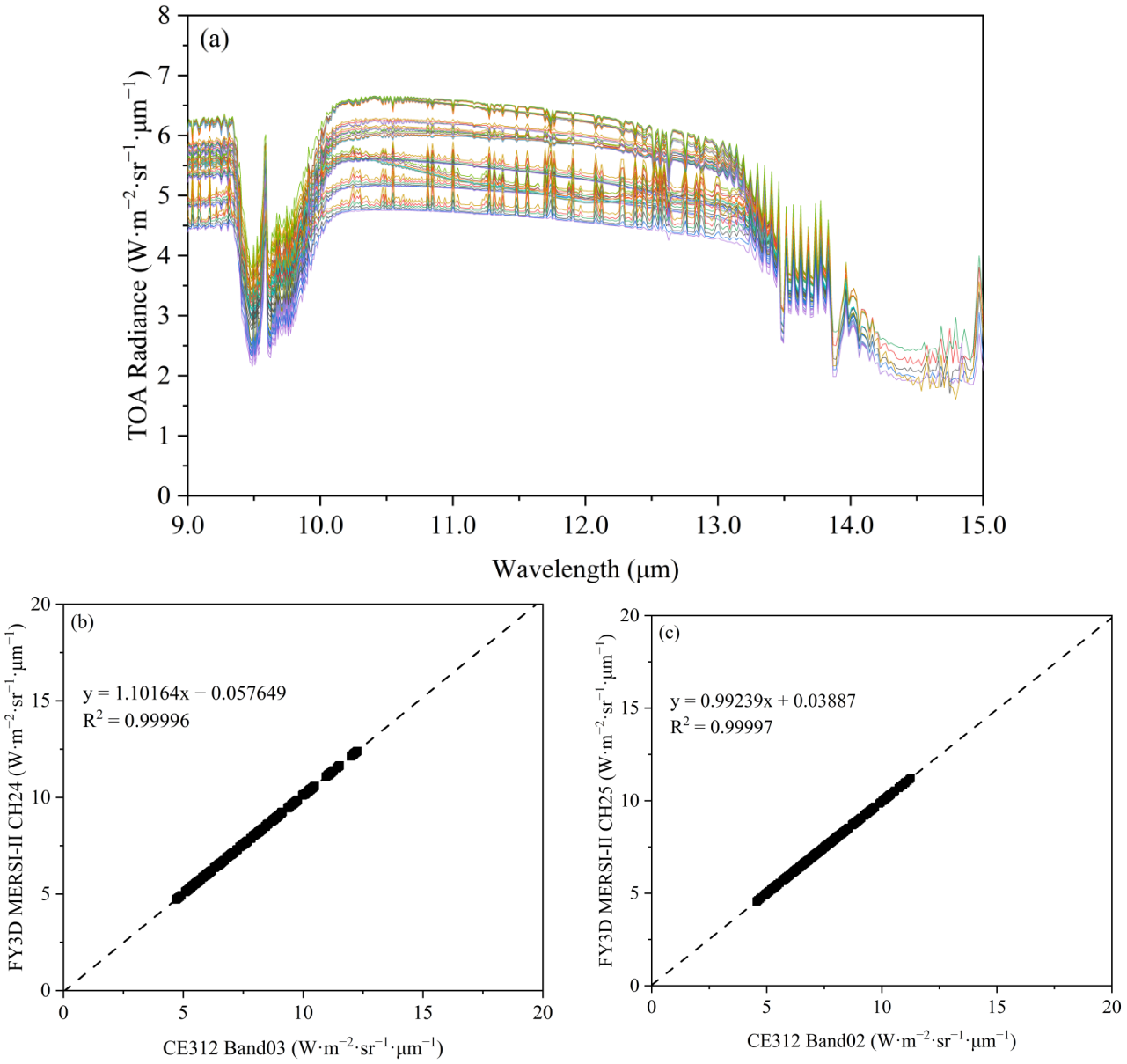

Figure 5. Spectral matching for thermal infrared channels of the FY−3D MERSI-II with the corresponding bands of the CE312–1N (**b**,**c**) by convolving the top-of-atmosphere (TOA) radiance (**a**) with the relative spectral response (RSR).

Table 2. Input parameters of moderate resolution atmospheric transmission (MODTRAN) 4.2 for the path radiance and the transmittance calculation on August 18 and August 20.

Date	Parameters	
	18 August 2019	**20 August 2019**
Time (UTC)	06:34:00	05:56:10
Solar Zenith	28.470°	28.460°
Solar Azimuth	−145.770°	−149.190°
Satellite Zenith	21.334°	37.430°
Satellite Azimuth	261.505°	26.130°
Ground Altitude	2.360 km	2.360 km
AOD@550nm	0.167	0.239

3.4. The Derivation of the Atmospheric Effects by MODTRAN Simulation

The atmospheric effects propagated from the land surface to the entrance aperture of the TIR sensors were quantified by the atmospheric transfer code (MODTRAN 4.2). First, the atmospheric profiles were measured by the radiosonde system during the satellite overpass, including elevation, air temperature, relative humidity, wind speed, and wind velocity. The radiosonde system manufactured by VAISALA consists of the radiosonde sensor RS90 and a balloon. An hour before the FY3D overpass, the balloon was released. According to the weather conditions, atmospheric profiles on August 18 and August 20 were collected to examine the atmospheric effects (Figure 6). The water vapor changed at the elevation between 5 km and 7 km because of the thin cirrus cloud near the calibration site. These were replaced by the mid-latitude summer profile provided by the MODTRAN code to improve the radiometric calibration accuracy. Then, MODTRAN simulations were conducted with the input parameters from the viewing geometries (i.e., solar zenith, satellite zenith, and relative azimuth), surface air temperature, and the atmospheric profiles. The influence of the atmosphere on the surface emitted radiance propagated from the land surface to the sensors' aperture was calculated by convolving the RSR of the MERSI-II bands with the path radiance and the transmittance profile, respectively. The equivalent path radiance and transmittance were generated for channel 24 and channel 25 of the FY3D MERSI-II, and were further used to evaluate the radiometric calibration accuracy of the FY3D TIR channels. Finally, the vicarious calibration coefficients were derived by combining the radiance results from the MODTRAN simulation and the deep-space view.

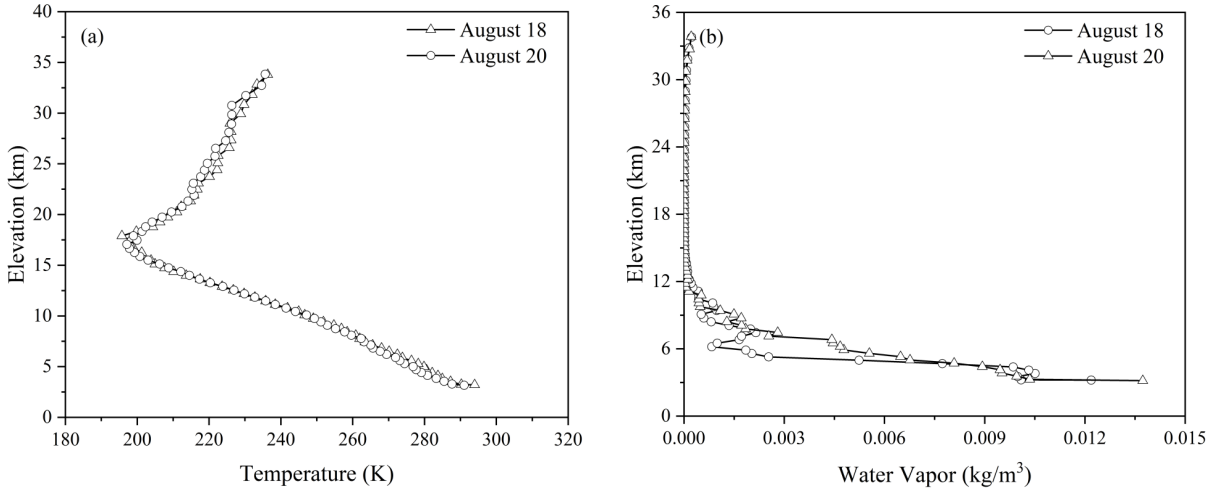

Figure 6. The atmospheric profiles. (**a**): the atmospheric temperature and (**b**): the water vapor content measured by the radiosonde system.

4. Results and Discussion

4.1. Calibration Results of the FY3D MERSI-II TIR Channels

Generally, the FY3D MERSI-II works well in orbit according to our field calibration analysis. The difference between the simulated brightness temperature and satellite-based brightness temperature was less than −0.3461 K and −0.7220 K for channel 24 on 18 and 20 August, respectively, while it increased to −0.4604 K and −1.0362 K for channel 25 on 18 and 20 August, respectively (Table 3). Thin cloud contamination may be responsible for the larger difference when the synchronous in-situ experiment was conducted on August 20 [30]. The cross-calibration between the FY−3A/B MERSI and the Terra/Aqua Moderate Resolution Imaging Spectroradiometer (MODIS), as well as the meteorological operational satellite-A/infrared atmospheric sounding interferometer (METOP-A/IASI) indicates that the bright temperature variation of the MERSI is close to that of the MODIS, with the bias mainly being less than 1 K [48]. The radiometric calibration accuracy of the

MERSI-II is higher than that of the MERSI by 0.5 K due to its more advanced onboard radiometric calibrator system [39].

Table 3. The difference between the simulated brightness temperature and satellite-based brightness temperature before and after spectral matching.

	Item	18 August		20 August	
		Channel 24	Channel 25	Channel 24	Channel 25
Before Spectral Matching	At-Sensor Radiance mW/(m²·sr·cm⁻¹)	93.209	108.587	93.177	108.345
	At-Sensor BT (K)	289.105	289.552	289.083	289.398
	Raw BT (K)	289.734	288.589	289.336	287.859
	Difference (K)	0.629	−0.964	0.253	−1.539
After Spectral Matching	At-Sensor Radiance mW/(m²·sr·cm⁻¹)	94.680	107.800	94.647	107.559
	At-Sensor BT (K)	290.080	289.049	290.058	288.895
	Raw BT (K)	289.734	288.589	289.336	287.859
	Difference (K)	−0.346	−0.460	−0.722	−1.036

In order to further validate the calibration results, we calculated the vicarious calibration coefficients for channels 24 and 25 of the MERSI-II on August 18 and 20, respectively (Figure 7). Generally, similar vicarious calibration coefficients could be derived during the study period, such as the calibration slope ranging from 0.0104 on August 18 to 0.0107 on August 20 for channel 24, with the calibration bias ranging from −3.143 K to −3.266 K. Meanwhile, the calibration slope and bias of channel 25 are similar to that of channel 24, ranging from 0.0103 to 0.0106 and −2.814 K to −2.943 K, respectively. The relative deviation of the calibration slope and bias is less than 1.43% and 1.92% for channel 24, with an increase to 1.44% and 2.24% for channel 25, respectively. The poor atmospheric conditions may be responsible for the large difference in those coefficients found between August 18 and 20 (Figure 6). The simulation analysis suggests that the aerosol optical depth (AOD) increase from 0.1680 to 0.2391 caused an at-sensor brightness temperature decrease by 0.169 K for channel 24 and 0.133 K for channel 25, respectively. The uniform relative spectral response of the detector array resulted in a higher brightness temperature bias by 2 K [36]. The normalized relative spectral response of the FY3D MERSI-II from pre-launch measurements may also influence the radiometric calibration result [36,49]. The large decrease in bias was mainly caused by the different space view DN, while the radiance was found to not be sensitive to the variation of the bias coefficient [50]. Thus, our results indicate that the vicarious experiment conducted on August 18 and August 20 is reasonable for the calibration evaluation.

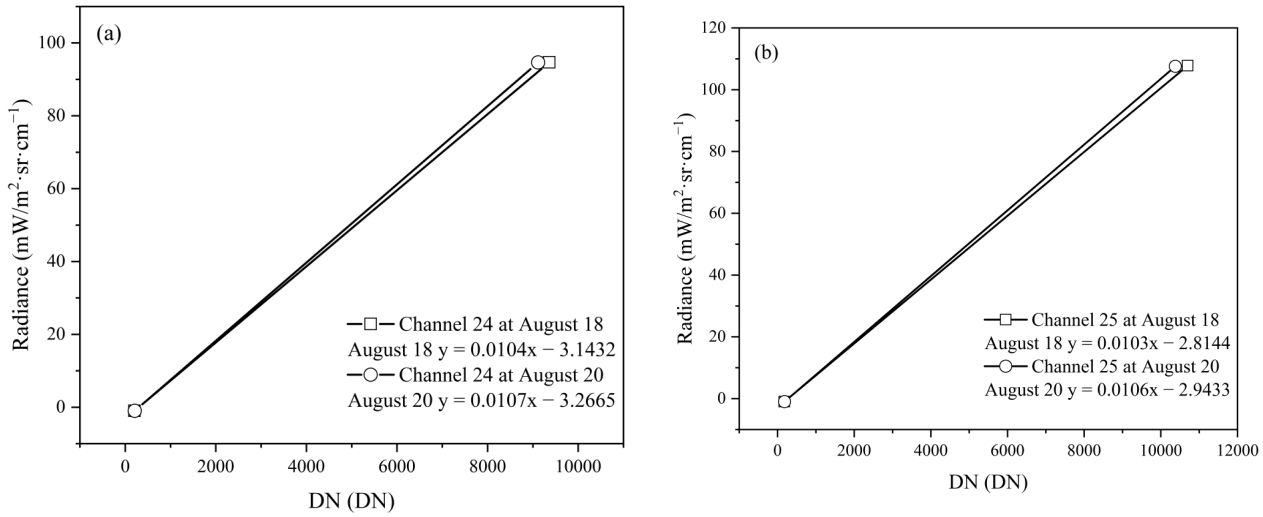

Figure 7. The calibration coefficients for the FY−3D MERSI-II channel 24 and channel 25 derived from the calibration campaign, (**a**) Channel 24, and (**b**) Channel 25.

4.2. Validation for the Vicarious Calibration Coefficient

In order to validate the radiometric calibration coefficients of the MERSI-II TIR channels, we compared the brightness temperature results derived from the vicarious calibration coefficients and operational calibration coefficients. We selected the stable surface targets as the validation sites, including Lake Nam and the Badain Jaran Desert on August 18 and Lake Kyrgyz and the Gobi Desert near Wuhai City on August 20 (Figure 8). A region, 1.50 km × 2.75 km, was selected for each site to extract the digital number and calculate the brightness temperature (Figure 8). We found that there are good agreements for the brightness temperature based on the official calibration coefficients and in-situ calibration coefficients for the MERSI-II TIR channels. The brightness temperature differences are −0.683 K (standard deviation = 0.507 K) for channel 24 and −0.480 K (standard deviation = 0.373 K) for channel 25 on August 18 (Figure 9). By contrast, the difference for those two channels on August 20 is a little larger, with −1.896 K (standard deviation = 0.529 K) for channel 24 and −2.372 K (standard deviation = 0.474 K) for channel 25. This phenomenon is possibly caused by the variation of the atmosphere during the FY3D overpass, leading to the differences in transmittance and path radiance and introducing some biases to the calculation of the in-situ calibration coefficients.

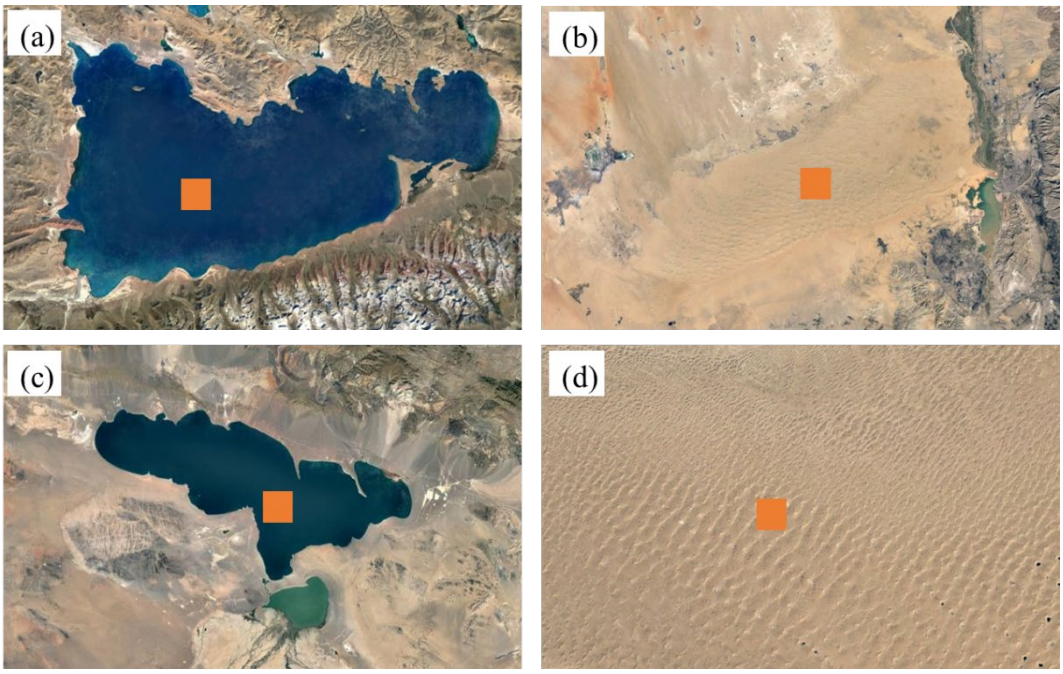

Figure 8. The selected sites for the validation of the FY−3D MERSI-II thermal infrared channels' in-situ radiometric calibration. (**a**) Lake Nam (30.718N, 90.624E) and (**b**) the Gobi Desert (39.647N, 106.257E) near Wuhai city were chosen for 18 August and (**c**) Lake Kyrgyz (49.168N, 93.277E) and (**d**) the Badain Jaran Desert (40.201N, 101.411E) were chosen for 20 August. Each selected region (red boxes) denotes the selected area used for validation.

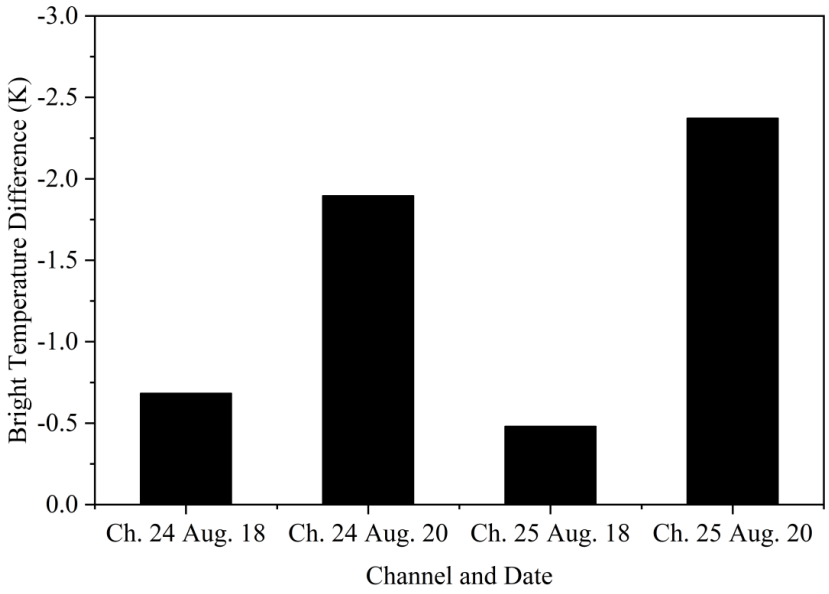

Figure 9. Validation results for the FY−3D MERSI-II's channel 24 and channel 25 for 18 August and 20 August.

4.3. Uncertainties About Calibration Analysis

The cirrus optical depth and the ice particle size distribution of the cirrus cloud cannot be measured accurately, which results in the bias of 0.310 K and 0.320 K for the radiometric accuracy of the MODIS band 31 and 32, respectively [30]. It is necessary to check the image data manually to get rid of the regions influenced by the cirrus cloud, including the stable distribution of the brightness temperature over those lake surfaces [28,35]. Water vapor is the most important variable for altering the long-wave radiation absorption [51] and its variation in an atmospheric profile introduces errors in the at-sensor radiance

propagation [31], such as a 10% error in the water vapor profile result in the at-sensor brightness temperature bias of 0.1 K for the MODIS band 31 (10.780–11.280 μm) [31,51]. We conducted a sensitivity analysis about the brightness temperature change at different levels of water vapor content using a MODTRAN simulation and the result shows that the water vapor content variation is positively related to the brightness temperature bias. For example, a 1.0g/m^3 variation caused a 1.0 K and 0.6 K brightness temperature (BT) bias in channel 24 and channel 25, respectively (Figure 10). When the water vapor reaches 4.0 g/m^3, the difference between the image-based and the simulated brightness temperature is stable for channel 24 and 25. In order to eliminate the influence of water vapor on long-wave radiation, the FY−3D MERSI-II specified two independent thermal infrared bands centered at 10.8 μm and 12.0 μm, which are similar to the specifications of the thermal bands of the Terra/MODIS and the Landsat−8/TIR [36,52,53].

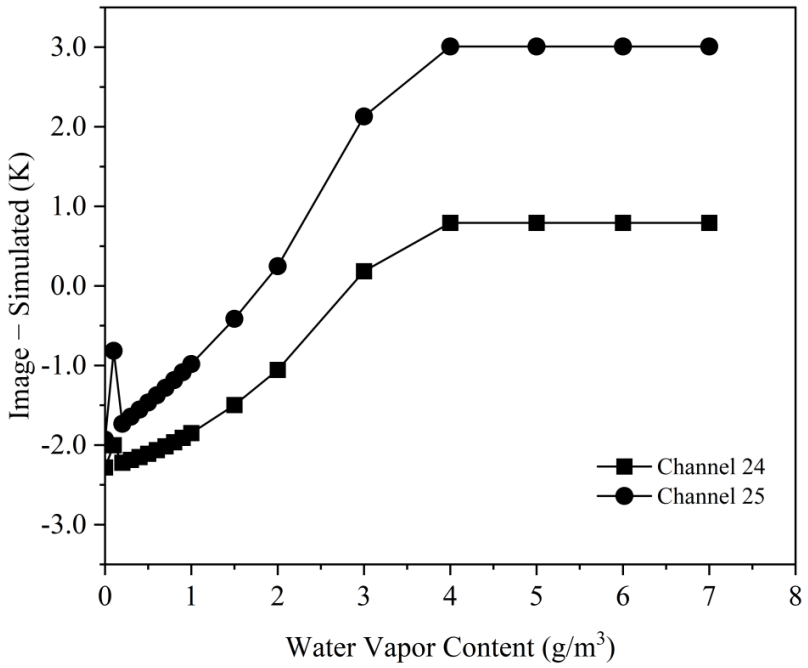

Figure 10. Sensitivity analysis for the variation of the brightness temperature bias induced by water vapor content using the MODTRAN code.

A difference in the relative spectral responses between the in-situ radiometers and the satellite TIR sensors will also introduce uncertainties in accurate radiometric calibration and spectral matching is essential to improve the accuracy of radiometric calibration [13,45,47]. This study employed the spectral matching factors from the atmospheric transfer simulation to reduce the RSR discrepancy and the difference was obviously improved after the spectral matching for channel 24 and channel 25 (Table 3); the accuracy increased by 44.98%, from 0.629 K to −0.346 K, on August 18, and from 0.253 K to −0.722 K on August 20 for channel 24. For channel 25, the difference decreased by 52.23%, from −0.964 K to −0.46044 K, on August 18, and 32.67%, from −1.539 K to −1.036 K, on August 20. Spectral matching improved the at-sensor brightness temperature by about 0.970 K for channel 24 and 0.50 K for channel 25. The results show that the spectral matching between different sensors can effectively reduce the discrepancy caused by the RSR in the vicarious radiometric calibration.

5. Conclusions

The radiometric calibration status of the FY3D MERSI-II TIR channels (channel 24 and 25) was evaluated by field experiments at Lake Qinghai from August 16 to 22, 2019. The skin

temperature of the lake surface was recorded by the CE312-N1 mounted on a USV, while the aerosol optical depth and the atmospheric profiles were collected from the radiosonde system and other instruments mounted near the calibration site. The at-sensor radiances were predicted by the MODTRAN code by considering the viewing geometries, atmospheric profiles, and surface temperature as the input parameters. Spectral matching based on the MODTRAN simulations was also adopted to reduce the discrepancy caused by the RSR in the radiometric calibration analysis. The difference between the simulated brightness temperature and the satellite-based brightness temperature was less than −0.346 K and −0.722 K for channel 24 on August 18 and 20, while it increased to −0.460 K and −1.036 K for channel 25 on August 18 and 20, respectively. The vicarious radiometric calibration coefficients were also derived based on the deep-space view and the field experiments for channel 24 and channel 25 of the FY3D MERSI-II; the relative deviation of the calibration slope and bias is less than 1.43% and 1.92% for channel 24, respectively, while it increases to 1.44% and 2.24% for channel 25, respectively. According to the validation analysis on other stable surfaces (lake or desert), the vicarious calibration coefficients are in good agreement with the official calibration coefficients. Therefore, our results indicate that the FY3D MERSI-II TIR channels work well within the first two years of operation. The water vapor and RSR mismatch have altered the calibration accuracy with 1 K and 0.6 K of BT bias in channel 24 and channel 25, respectively, by a 1 g/m^3 variation in water vapor, and the at-sensor brightness temperature is closer to the predicted brightness temperature after spectral matching.

Author Contributions: Conceptualization, Y.H., Y.Z. and L.Y.; investigation, Y.H., Y.Z. and L.Y.; data collection, Y.H., L.Y., Y.Z., L.Z. and Y.S.; writing and original draft, L.Y.; writing—reviewing and editing, Y.H., Y.Z., C.D. and L.Y.; methodology, L.Y.; project administration, X.-M.L., J.L. and Y.Z. All authors have read and agreed to the published version of the manuscript.

Funding: This work was supported by the CAS Strategic Priority Research Program (XDA19010402), the Technical Pre-research Project of Civil Aerospace (D040401), and the National Key Research and Development Program of China (2017YFB0502900).

Data Availability Statement: No new data were created or analyzed in this study. Data sharing is not applicable to this article.

Acknowledgments: The authors appreciate the help of Hongbin Chen's USV group from the Key Laboratory of Middle Atmosphere and Global Environment Observation (LAGEO), the Institute of Atmospheric Physics, and the Chinese Academy of Sciences.

Conflicts of Interest: The authors declare no conflicts of interest.

References

1. Russell, J.E.; Haigh, J.D. Effect of Cloud Vertical Inhomogeneity on the Retrieval of Cirrus Cloud Temperature and Infrared Optical Depth Using the ASTR. *J. Atmos. Sci.* **1999**, *56*, 2601–2612, doi:10.1175/1520–0469(1999)0562.0.co;2.
2. Jedlovec, G.J.; Haines, S.L.; Lafontaine, F.J. Spatial and Temporal Varying Thresholds for Cloud Detection in GOES Imagery. *IEEE Trans. Geosci. Remote Sens.* **2008**, *46*, 1705–1717, doi:10.1109/tgrs.2008.916208.
3. Zhang, X.; Zhong, T.; Feng, X.; Wang, K. Estimation of the relationship between vegetation patches and urban land surface temperature with remote sensing. *Int. J. Remote Sens.* **2009**, *30*, 2105–2118, doi:10.1080/01431160802549252.
4. Alcântara, E.H.; Stech, J.L.; Lorenzzetti, J.A.; Bonnet, M.-P.; Casamitjana, X.; Assireu, A.T.; Novo, E.M.L.D.M. Remote sensing of water surface temperature and heat flux over a tropical hydroelectric reservoir. *Remote Sens. Environ.* **2010**, *114*, 2651–2665, doi:10.1016/j.rse.2010.06.002.
5. Silvestro, F.; Gabellani, S.; Delogu, F.; Rudari, R.; Boni, G. Exploiting remote sensing land surface temperature in distributed hydrological modelling: The example of the Continuum model. *Hydrol. Earth Syst. Sci.* **2013**, *17*, 39–62, doi:10.5194/hess–17–85–2013.
6. Orsini, A.; Calzolari, F.; Georgiadis, T.; Levizzani, V.; Nardino, M.; Pirazzini, R.; Rizzi, R.; Sozzi, R.; Tomasi, C. Parameterisation of surface radiation flux at an Antarctic site. *Atmos. Res.* **2000**, *54*, 245–261, doi:10.1016/s0169–8095(00)00047–8.
7. Kandel, R.; Viollier, M. Observation of the Earth's radiation budget from space. *Comptes Rendus Geosci.* **2010**, *342*, 286–300, doi:10.1016/j.crte.2010.01.005.
8. Hu, T.; Cao, B.; Du, Y.; Li, H.; Wang, C.; Bian, Z.; Sun, D.; Liu, Q. Estimation of Surface Upward Longwave Radiation Using a Direct Physical Algorithm. *IEEE Trans. Geosci. Remote Sens.* **2017**, *55*, 4412–4426, doi:10.1109/tgrs.2017.2692261.

9. Ohring, G.; Tansock, J.; Emery, W.J.; Butler, J.; Flynn, L.E.; Weng, F.; Germain, K.S.; Wielicki, B.; Cao, C.; Goldberg, M.; et al. Achieving satellite instrument calibration for climate change. *Trans. Am. Geophys. Union.* **2013**, *88*, 136, doi:10.1029/2007eo110015.
10. Li, Z.-L.; Tang, B.-H.; Wu, H.; Ren, H.; Yan, G.; Wan, Z.; Trigo, I.F.; Sobrino, J.A. Satellite-derived land surface temperature: Current status and perspectives. *Remote Sens. Environ.* **2013**, *131*, 14–37, doi:10.1016/j.rse.2012.12.008.
11. Gao, S.; Li, Z.; Chen, Q.; Zhou, W.; Lin, M.; Yin, X. Inter-Sensor Calibration between HY−2B and AMSR2 Passive Microwave Data in Land Surface and First Result for Snow Water Equivalent Retrieval. *Sensors* **2019**, *19*, 5023, doi:10.3390/s19225023.
12. Baraldi, A. Impact of Radiometric Calibration and Specifications of Spaceborne Optical Imaging Sensors on the Development of Operational Automatic Remote Sensing Image Understanding Systems. *IEEE J. Sel. Top. Appl. Earth Obs. Remote Sens.* **2009**, *2*, 104–134, doi:10.1109/jstars.2009.2023801.
13. Gao, H.; Gu, X.; Yu, T.; Sun, Y.; Liu, Q. Cross-Calibration of GF−1 PMS Sensor with Landsat 8 OLI and Terra MODIS. *IEEE Trans. Geosci. Remote Sens.* **2016**, *54*, 4847–4854, doi:10.1109/tgrs.2016.2552242.
14. Gu, X.; Tian, G.; Yu, T.; Li, X.; Gao, H.; Xie, Y. *Principle and Method of Radiometric Calibration for Space Optical Remote Sensors*; Science Press: Beijing, China, 2013.
15. Zhang, Y.; Zheng, Z.; Hu, X.; Rong, Z.; Zhang, L. Lake Qinghai: Chinese site for radiometric calibration of satellite infrared remote sensors. *Remote Sens. Lett.* **2013**, *4*, 315–324, doi:10.1080/2150704x.2012.728298.
16. Sayer, A.M.; Hsu, N.C.; Bettenhausen, C.; Jeong, M.; Meister, G. Effect of MODIS Terra radiometric calibration improvements on Collection 6 Deep Blue aerosol products: Validation and Terra/Aqua consistency. *J. Geophys. Res. Atmos.* **2015**, *120*, 12,157–, doi:10.1002/2015jd023878.
17. Kim, W.; He, T.; Wang, D.; Cao, C.; Liang, S. Assessment of Long-Term Sensor Radiometric Degradation Using Time Series Analysis. *IEEE Trans. Geosci. Remote Sens.* **2013**, *52*, 2960–2976, doi:10.1109/tgrs.2013.2268161.
18. Wang, W.; Cao, C. Assessing the VIIRS RSB Calibration Stability Using Deep Convective Clouds; In *Earth Observing Missions and Sensors: Development, Implementation, and Characterization III*; SPIE: Bellingham, WA, USA, 2014; Volume 9264, p. 926410.
19. Wang, W.; Cao, C. DCC Radiometric Sensitivity to Spatial Resolution, Cluster Size, and LWIR Calibration Bias Based on VIIRS Observations. *J. Atmos. Ocean. Technol.* **2015**, *32*, 48–60, doi:10.1175/jtech-d−14–00024.1.
20. Wang, W.; Cao, C. Monitoring the NOAA Operational VIIRS RSB and DNB Calibration Stability Using Monthly and Semi-Monthly Deep Convective Clouds Time Series. *Remote Sens.* **2016**, *8*, 32, doi:10.3390/rs8010032.
21. Bhatt, R.; Doelling, D.R.; Scarino, B.R.; Gopalan, A.K.S.; Haney, C.O. Toward consistent radiometric calibration of the NOAA AVHRR visible and near-infrared data record. In *Earth Observing Systems XX*; SPIE: Bellingham, WA, USA, 2015; Volume 9607, p. 960703.
22. Qiu, S.; Shao, X.; Cao, C.; Wang, W. Vicarious Validation of Straylight Correction for VIIRS Day/Night Band Using Dome-C. In *Earth Observing Systems XX*; SPIE: Bellingham, WA, USA, 2015; Volume 9607, p. 96072H, doi:10.1117/12.2188401.
23. Brown, S.W.; Flora, S.J.; Feinholz, M.E.; Yarbrough, M.A.; Houlihan, T.; Peters, D.; Kim, Y.S.; Mueller, J.L.; Johnson, B.C.; Clark, D.K. The marine optical buoy (MOBY) radiometric calibration and uncertainty budget for ocean color satellite sensor vicarious calibration. In *Sensors, Systems, and Next-Generation Satellites XI*; SPIE: Bellingham, WA, USA, 2007; p. 67441M.
24. Elyouncha, A.; Acheroy, M. Radiometric cross-calibration of spaceborne scatterometers: First results. In *Remote Sensing of the Ocean, Sea Ice, and Large Water Regions 2009*; SPIE: Bellingham, WA, USA, 2009; Volume 7473, p. 74730B.
25. Hu, X.; Zhang, Y.; Liu, Z.; Huang, Y.; Qiu, K.; Wang, Y.; Zhu, X.; Rong, Z. Optical characteristics of China Radiometric Calibration Site for Remote Sensing Satellite Sensors (CRCSRSSS). In *Hyperspectral Remote Sensing of the Land and Atmosphere*; SPIE: Bellingham, WA, USA, 2001; Volume 4151, doi:10.1117/12.416994.
26. Barry, P.; Jarecke, P.J.; Pearlman, J.; Jupp, D.L.B.; Lovell, J.; Campbell, S. Radiometric calibration validation of the Hyperion instrument using ground truth at a site in Lake Frome, Australia. In *Imaging Spectrometry VII*; SPIE: Bellingham, WA, USA, 2002; Volume 4480.
27. Li, Z.; Xingfa, G.; Yuxiang, Z.; Tao, Y.; Liangful, C.; Hui, G.; HongYan, H. A vicarious calibration for thermal infrared bands of TERRA-MODIS sensor using a new calibration test site-lake dali, China. In Proceedings of the 2007 IEEE International Geoscience and Remote Sensing Symposium, Barcelona, Spain, 23–28 July 2007.
28. Wołczyński, W.; Guzik, E.; Wajda, W.; Jedrzejczyk, D.; Kania, B.; Kostrzewa, M. Cet in Solidifying Roll—Thermal Gradient Field Analysis. *Arch. Met. Mater.* **2012**, *57*, 105–117, doi:10.2478/v10172–011–0159–9.
29. Williams, G.; Douglas, J. Comments on Cretaceous climatic equability in polar regions. *Palaeogeogr. Palaeoclim. Palaeoecol.* **1985**, *49*, 355–357, doi:10.1016/0031–0182(85)90061–6.
30. Wan, Z.; Zhang, Y.; Li, Z.-L.; Wang, R.; Salomonson, V.V.; Yves, A.; Bosseno, R.; Hanocq, J.F. Preliminary estimate of calibration of the moderate resolution imaging spectroradiometer thermal infrared data using Lake Titicaca. *Remote Sens. Environ.* **2002**, *80*, 497–515, doi:10.1016/s0034–4257(01)00327–3.
31. Hook, S.J.; Vaughan, R.G.; Tonooka, H.; Schladow, S.G. Absolute Radiometric In-Flight Validation of Mid Infrared and Thermal Infrared Data from ASTER and MODIS on the Terra Spacecraft Using the Lake Tahoe, CA/NV, USA, Automated Validation Site. *IEEE Trans. Geosci. Remote Sens.* **2007**, *45*, 1798–1807, doi:10.1109/tgrs.2007.894564.
32. Hook, S.; Chander, G.; Barsi, J.; Alley, R.; Abtahi, A.; Palluconi, F.; Markham, B.L.; Richards, R.; Schladow, S.; Helder, D. In-flight validation and recovery of water surface temperature with Landsat−5 thermal infrared data using an automated high-altitude lake validation site at Lake Tahoe. *IEEE Trans. Geosci. Remote Sens.* **2004**, *42*, 2767–2776, doi:10.1109/tgrs.2004.839092.
33. Schott, J.R.; Hook, S.J.; Barsi, J.A.; Markham, B.L.; Miller, J.; Padula, F.P.; Raqueno, N.G. Thermal infrared radiometric calibration of the entire Landsat 4, 5, and 7 archive (1982–2010). *Remote Sens. Environ.* **2012**, *122*, 41–49, doi:10.1016/j.rse.2011.07.022.

34. Dong, C.; Yang, J.; Zhang, W.; Yang, Z.; Lu, N.; Shi, J.; Zhang, P.; Liu, Y.; Cai, B. An Overview of a New Chinese Weather Satellite FY−3A. *Bull. Am. Meteorol. Soc.* **2009**, *90*, 1531–1544, doi:10.1175/2009bams2798.1.
35. Yang, J.; Zhang, P.; Lu, N.; Yang, Z.; Shi, J.; Dong, C. Improvements on global meteorological observations from the current Fengyun 3 satellites and beyond. *Int. J. Digit. Earth* **2012**, *5*, 251–265, doi:10.1080/17538947.2012.658666.
36. Xu, N.; Chen, L.; Hu, X.; Zhang, L.; Zhang, P. Assessment and Correction of on-Orbit Radiometric Calibration for FY−3 VIRR Thermal Infrared Channels. *Remote Sens.* **2014**, *6*, 2884–2897, doi:10.3390/rs6042884.
37. National Satellite Meteorological Center China Meteorological Administration. Available online: http://www.nsmc.org.cn/en/nsmc/channels/FY−3SeriesSatellites.html (accessed on 1 September 2019).
38. Jiang, J.; Wang, M.; Ju, S.; Xi, J. Land Surface Temperature Retrieval from FY−3D MERSI−2 Data in the Arid/Semi-Arid Area. *Adv. Geosci.* **2019**, *9*, 693–702, doi:10.12677/ag.2019.98074.
39. Xu, N.; Niu, X.; Hu, X.; Wang, X.; Wu, R.; Chen, S.; Chen, L.; Sun, L.; Ding, L.; Yang, Z.; et al. Prelaunch Calibration and Radiometric Performance of the Advanced MERSI II on FengYun−3D. *IEEE Trans. Geosci. Remote Sens.* **2018**, *56*, 4866–4875, doi:10.1109/tgrs.2018.2841827.
40. Tong, J.; Déry, S.J.; Chen, Y.; Hu, B. An alternative method for in-flight absolute radiometric calibration of thermal infrared channels of Chinese geostationary meteorological satellites. *Int. J. Remote Sens.* **2010**, *31*, 791–803, doi:10.1080/01431160902897841.
41. Zhang, Y.; Gu, X.; Yu, T.; Li, X.; Li, X. In-flight method for CBERS−02 IRMSS thermal channel absolute radiometric calibration at Lake Qinghai (China). *IEEE Trans. Geosci. Remote Sens.* **2005**, *3*, 2227–2230, doi:10.1109/igarss.2005.1526463.
42. Zhang, Y.; Gu, X.; Yu, T.; Li, X. Radiometric cross-calibration of CBERS−02 IRMSS thermal channel against TERRA MODIS. In *Sensors, Systems, and Next-Generation Satellites IX*; SPIE: Bellingham, WA, USA, 2005; Volume 5978, p. 59781V.
43. Brogniez, G.E.R.; Pietras, C.; Legrand, M.; Dubuisson, P.; Haeffelin, M. A high-accuracy multiwavelength radiometer for in situ measurements in the thermal infrared. Part II: Behavior in field experiments. *J. Atmos. Ocean. Technol.* **2003**, *20*, 1023–1033, doi:10.1175/1520–0426(2003)202.0.CO;2.
44. National Satellite Meteorological Center China Meteorological Administration. FY3D Data Usage Guide. Available online: http://satellite.nsmc.org.cn/ (accessed on 12 November 2019).
45. Chander, G.; Mishra, N.; Helder, D.L.; Aaron, D.; Choi, T.; Angal, A.; Xiong, X. Use of EO−1 Hyperion data to calculate spectral band adjustment factors (SBAF) between the L7 ETM+ and Terra MODIS sensors. In Proceedings of the IEEE International Geoscience and Remote Sensing Symposium, Honolulu, HI, USA, 25–30 July 2010; doi:10.1109/IGARSS.2010.5652746.
46. Xu, N.; Hu, X.-Q.; Chen, L.; Zhang, Y.; Hu, J.-Y.; Sun, L. On-Orbit Radiometric Calibration Accuracy of FY−3A MERSI Thermal Infrared Channel. *Spectrosc. Spectr. Anal.* **2014**, *34*, 3429–3434, doi:10.3964/j.issn.1000–0593(2014)12–3429−06.
47. Chander, G.; Mishra, N.; Helder, D.; Aaron, D.; Angal, A.; Choi, T.; Xiong, X.; Doelling, D.R. Applications of Spectral Band Adjustment Factors (SBAF) for Cross-Calibration. *IEEE Trans. Geosci. Remote Sens.* **2013**, *51*, 1267–1281, doi:10.1109/tgrs.2012.2228007.
48. Li, Y.; Wu, J.; Fang, Y. Cross-Calibration of FY−3A/VIRR Thermal Infrared Channel with TERRA/MODIS. *J. Atmos. Environ. Optics.* **2016**, *11*, 204–210, doi:10.3969/j.issn.1673–6141.2016.03.006.
49. Hu, X.Q.; Zhang, L.Y.; Zheng, Z.J.; Zhang, Y.; Sun, L.; Ding, L.; Huang, X.X. FY−3A multi-detector radiometric calibration for infrared band of medium resolution spectral imager. *Optics. Precis. Eng.* **2010**, *18*, 1972–1980, doi:10.3788/OPE.20101809.1972.
50. Chen, Y.; Sun, K.; Li, D.; Bai, T.; Huang, C. Radiometric Cross-Calibration of GF−4 PMS Sensor Based on Assimilation of Landsat−8 OLI Images. *Remote Sens.* **2017**, *9*, 811, doi:10.3390/rs9080811.
51. Wan, Z.; Li, Z.-L. A physics-based algorithm for retrieving land-surface emissivity and temperature from EOS/MODIS data. *IEEE Trans. Geosci. Remote Sens.* **1997**, *35*, 980–996, doi:10.1109/36.602541.
52. Xiong, X.; Chiang, K.; Wu, A.; Barnes, W.; Guenther, B.; Salomonson, V.V. Multiyear On-Orbit Calibration and Performance of Terra MODIS Thermal Emissive Bands. *IEEE Trans. Geosci. Remote Sens.* **2008**, *46*, 1790–1803, doi:10.1109/tgrs.2008.916217.
53. Barsi, J.A.; Schott, J.R.; Hook, S.J.; Raqueno, N.G.; Markham, B.L.; Radocinski, R.G. Landsat−8 Thermal Infrared Sensor (TIRS) Vicarious Radiometric Calibration. *Remote Sens.* **2014**, *6*, 11607–11626, doi:10.3390/rs61111607.